

# General-stacking-fault energies in highly strained metallic environments: *Ab initio* calculations

C. Brandl, P. M. Derlet, and H. Van Swygenhoven

Paul Scherrer Institute, ASQ/NUM, Materials Science and Simulation, PSI-Villigen CH-5232, Switzerland

(Received 1 June 2007; published 29 August 2007)

Past work has shown that the generalized-stacking-fault surface energy (GSFE) curve, which represents the energy dependency of rigidly shearing an fcc crystal at a (111) plane along a  $[-1-12]$  slip direction, can provide invaluable information on the nature of the dislocation activity in nanocrystalline Ni, Al, and Cu. Atomistic simulations have also revealed the complex localized strain environment in which nanocrystalline dislocation nucleation occurs. Using the density functional theory method, the present work investigates the role of an imposed isotropic and simple shear strain field on the shape of a GSFE curve for Al, Cu, and Ni, and, in particular, how this affects the ratio of the stable to unstable stacking fault surface energy. The results are discussed in terms of second and third order elasticity theories.

DOI: 10.1103/PhysRevB.76.054124

PACS number(s): 61.72.Nn, 62.20.Fe, 61.46.Hk, 71.15.Mb

## I. INTRODUCTION

An important material parameter is the so-called generalized-stacking-fault energy (GSFE) curve, which represents the energy dependency of rigidly shearing a crystal at a (111) plane along a  $[-1-12]$  slip direction,<sup>1,2</sup> and gives information about the shear properties of a perfect crystal and therefore insight into a material's ideal shear strength as originally proposed by Frenkel.<sup>3</sup> Rice has employed the extrema points of the GSFE curve to study dislocation nucleation at a crack tip.<sup>4</sup> Although GSFE curves are experimentally not accessible, with the advent of empirical and *ab initio* atomistic simulation methods, the GSFE curve has been the focus of considerable attention in the simulations of plasticity of bulk crystalline materials.<sup>5-8</sup>

The plastic deformation of metallic nanocrystalline (nc) materials is believed to be mediated by partial dislocations that are nucleated at grain boundaries (GBs), propagate through the grains, and eventually are absorbed in neighboring GB regions.<sup>9</sup> This viewpoint has been suggested by atomistic simulation of computer generated fcc metallic nc structures<sup>10-15</sup> and is supported by *in situ* x-ray diffraction experiments that can probe the dynamics of plasticity.<sup>16,17</sup> In these simulations, the GSFE curve has been used to clarify why simulations performed for Al show full dislocations traveling across the grain leaving no dislocation debris in their wake, while for Cu and Ni only leading partials traveling across the grain are seen leaving behind an extended stacking fault that experimentally has not been observed.<sup>18-20</sup> In particular, it was demonstrated that, given the nucleation

of a leading partial, the probability that a second trailing partial is nucleated depends on the stable and unstable stacking fault surface energy density for the empirical potential used. If the stable to unstable stacking fault ratio is close to 1, then the likelihood of observing full dislocations within the nanosecond time frame of a classical molecular dynamics simulation is high. If the ratio is low, the likelihood of seeing a full dislocation in a simulation is minimal.

The arguments presented in Ref. 18 that relate an empirical potential's GSFE curve to the resulting nature of dislocation activity within the nc system are, however, based on the rigid slip properties of unstrained fcc lattices with the implicit view that the results are transferable to highly strained environments. Detailed analysis of the atomistic configurations during loading has, however, shown that leading and trailing partial dislocations often nucleate in the vicinity of anomalous local stress intensities in the GB and that nucleation is usually followed by a subsequent relaxation and removal of the stress intensity.<sup>13-15</sup> Figure 1 displays an atomic cross section of a grain boundary region where in (a) the atoms are colored and/or shaded according to their local crystallinity:<sup>21</sup> gray (light gray) atoms are locally fcc, red (dark gray) locally hcp, green (dark gray) other 12 coordinated, and blue (dark gray) non-12 coordinated, (b) according to their local hydrostatic pressure and (c) according to their local deviatoric stress. The two latter quantities are the scalar invariants of the local stress tensor calculated according to the momentum conserving expression for the virial stress,<sup>22</sup> and have been used in the past work to investigate the stress signature of computer generated nc GBs.<sup>15,23</sup> Fig-

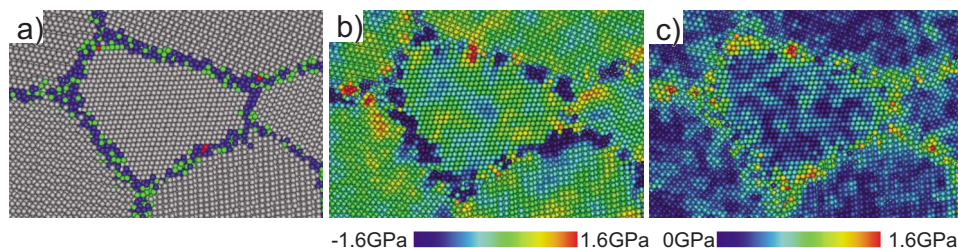


FIG. 1. (Color online) Atomic cross section of a computer generated nanocrystalline sample where atoms are colored and/or shaded according to (a) medium range order analysis, (b) local hydrostatic pressure, and (c) local deviatoric shear stress.

ure 1(a) provides an easy identification of where the GBs and grains are—the GBs are visualized by the nongray and/or dark regions. Inspection of the stress invariants reveals strong oscillations in the gigapascal range particularly close to the GB region: we note that a positive hydrostatic pressure represents tension. It is in such highly stressed regions that leading and trailing partial dislocations nucleate.

In the present work, *ab initio* calculation methods are used to calculate GSFE curves in highly strained environments. In particular, using density functional theory (DFT) the present paper investigates the role of an imposed isotropic and volume conserving simple shear strain field on the shape of a GSFE curve and, in particular, how this affects the ratio of the stable to unstable stacking fault surface energy densities for Al, Cu, and Ni. It is found that the conclusions made in Ref. 18 retain their validity in highly strained environments. The calculations also shed further light on the electronic origin of the important features of the GSFE curve and how they can be related to second and third order elasticities.

## II. CALCULATION AND RESULTS

For the calculations of the GSFE curves, the DFT code VASP was used, in which the pseudopotential originates from the projector augmented wave framework.<sup>24,25</sup> Convergence is reached within an error in total free energy of 0.01 meV for the electronic contributions and 0.1 meV for the atomic positions. To guarantee convergence within 0.1 meV/at., 72 irreducible  $k$  points and a 400 eV energy cutoff are chosen. For correct handling of the Fermi surface, the smearing method of Methfessel and Paxton was used.<sup>26</sup> To simulate ferromagnetic Ni, spin polarized simulations were performed. The orbital resolved local density of states (DOS) calculations were determined by projecting the wave functions derived from the converged charge densities onto local orbitals within the Wigner-Seitz radius. The simulation cells for the GSFE calculations are built up from 12 (111) layers via an *ABC* stacking to produce an fcc slab structure separated by a vacuum region. The GSFE curves are generated by ten equally spaced rigid shifts of the upper six (111) layers in the  $[-1-12]$  direction. For each rigid shift, the atomic positions are relaxed along the  $[111]$  direction by minimization of the Hellmann-Feynman forces on each atom. The atoms within the two (111) layers closest to each surface are held fixed during this relaxation. This type of calculation is repeated for several isotropic volume changes and for a number of volume conserving shear strains along the  $[-1-12]$  direction. These two strained environments were chosen to separately investigate the effect of changing the volume per atom which probes the effect of bond length and a simple shear distortion which probes the simplest shear distortion at a constant volume per atom.

### A. Generalized-stacking-fault curves

Figure 2 displays the calculated *ab initio* GSFE curves for Al, ferromagnetic (FM), and nonmagnetic (NM) Ni and Cu at zero pressure. Table I lists the corresponding unstable and

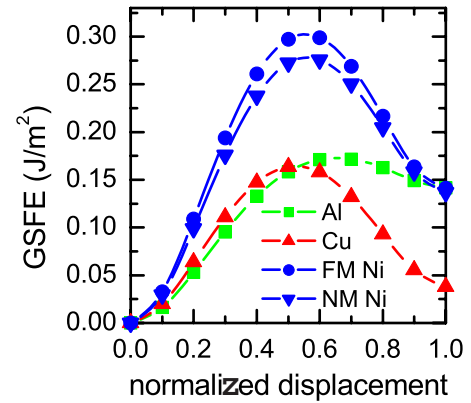


FIG. 2. (Color online) General-stacking-fault curves for magnetic and nonmagnetic Ni, Cu, and Al.

stable stacking fault energies along with other calculated values published in literature.<sup>7,27–32</sup> Figure 2 and Table I show that Cu has the lowest stable stacking fault energy, followed by Ni, and Al has the highest stable stacking fault energy. The addition of ferromagnetism in Ni raises the unstable stacking fault energy by  $\sim 20$  mJ/m<sup>2</sup> and the stable stacking fault energy by  $\sim 3$  mJ/m<sup>2</sup>. In terms of the unstable stacking fault energy, we see that Al does indeed have the lowest value relative to its stable stacking fault energy when compared to Cu and Ni, that is, a ratio closest to unity.

The stacking fault energy ordering across the three elements may be largely understood in terms of the energy of hcp and fcc phases. At a stacking fault, an *ABAB* stacking sequence exists resulting in the two (111) planes of the fault exhibiting a locally hcp nearest neighbor environment. The equilibrium stacking fault energy is therefore related to the energy difference between the bulk fcc and hcp phases,  $E_{\text{fcc-hcp}}$ , of that material with  $2E_{\text{fcc-hcp}} \approx E_{\text{sf}}$ . Such a relation has been established for the  $3d$ ,  $4d$ , and  $5d$  transition metal elements<sup>33</sup> and is a result of the short range nature of the transition metal  $d$ -state bonding. Since both fcc and hcp are close packed structures, the short range bonding environment differs only in the dihedral angle between nearest neighbors and therefore the  $d$ -state  $\pi$ - and  $\delta$ -type bondings are particularly sensitive to such a structural difference. Such angular dependent bondings become increasingly important in open shell systems and it is for this reason that Ni, with eight  $3d$  electrons, has a higher  $E_{\text{fcc-hcp}}$  energy than Cu which has a closed shell. For the case of trivalent Al, the dominant open shell bonding is seen to occur in the form of  $ss$ - $\sigma$ ,  $sp$ - $\sigma$ ,  $pp$ - $\sigma$ , and  $pp$ - $\pi$  bonding and also a component due to  $dd$ - $\pi$  and  $dd$ - $\delta$  bonding, leading to its own higher value of  $E_{\text{fcc-hcp}}$  and stacking fault energy.<sup>34</sup>

Figure 3 displays the GSFE curves for Al, Cu, and Ni as a function of isotropic volume change. For all three elements, the stable stacking fault energy decreases with increasing volume, a trend that can be understood by considering the volume dependence of  $E_{\text{fcc-hcp}}$ . Figure 4 plots the stable stacking fault energy versus the calculated  $2E_{\text{fcc-hcp}}$  for Al, Ni, and Cu for all volumes considered in Fig. 3. The resulting linear correlation clearly demonstrates the validity of the  $2E_{\text{fcc-hcp}}$  approach for Cu, Ni, and now for Al. There are, however, also some important differences: Cu and Ni are less

TABLE I. Unstable and/or stable stacking fault energies calculated in the present work for Al, Cu, and ferromagnetic Ni and previously published literature values. All values are given in  $\text{mJ}/\text{m}^2$ .

	Present work	Ogata <i>et al.</i> <sup>a</sup>	Denteneer and Soler <sup>b</sup>	Hartford <i>et al.</i> <sup>c</sup>	Zimmerman <i>et al.</i> <sup>d</sup>	Lu <i>et al.</i> <sup>e</sup>	Sun and Kaxiras <sup>f</sup>	Wright <i>et al.</i> <sup>g</sup>
Al	178/146	175/158	-/126	-/143	213/153	224/164	224/165	-/161
Cu	164/38	158/39			210/49			
Ni	278/137				350/183			

<sup>a</sup>Reference 7.

<sup>b</sup>Reference 27.

<sup>c</sup>Reference 28.

<sup>d</sup>Reference 29.

<sup>e</sup>Reference 30.

<sup>f</sup>Reference 31.

<sup>g</sup>Reference 32.

sensitive to volume changes than Al, with the latter's stacking fault energy changing more rapidly than  $2E_{\text{fcc-hcp}}$ . Since for the transition metals, it is  $d$ -state bonding that predominantly contributes to  $E_{\text{fcc-hcp}}$ , the electronic origin for this difference has to be found in the radial behavior of the Al interatomic interaction. Indeed, for Cu and Ni the dominant short range  $d$ -state bonding has an  $\sim R^{-5}$  range whereas in Al the  $s$ - $p$  bonding has an  $\sim R^{-2}$  range<sup>35</sup> that can also manifest itself in higher-order second and third nearest neighbor interactions that contribute also to  $E_{\text{fcc-hcp}}$ .<sup>36,37</sup>

With these considerations in mind, Fig. 5(a) now plots the unstable and stable stacking fault energies as a function of volume revealing that the unstable stacking fault energy dependency closely follows that of the stable stacking fault. This is particularly evident when the ratio of the two energies is plotted, as in Fig. 5(b), revealing a negligible change in the ratio for all three elements.

Figure 6 now displays the GSFE curves for a range of applied volume conserving shear strains in the  $[-1-12]$  direction. In these plots the elastic shear strain energy and the shear strain were added to the calculated GSFE values in order to be able to investigate nonlinear changes in the GSFE curves. The elastic strain energy was calculated using the *ab initio* derived elastic constants of each material with the formula  $\Delta E_e = \mu \gamma^2 / 2$  in which  $\mu = (C_{11} - C_{12} + C_{44}) / 3$  is the

elastic shear modulus in the slip plane and slip direction. Inspection of Fig. 6 reveals that by doing so, the GSFE curves for Cu and nonmagnetic Ni fall nicely on top of each other, indicating that the GSFE curve remains essentially unchanged with the imposition of a volume conserving shear strain field. For the case of magnetic Ni and Al, we see a change in the shape of the GSFE curves as a function of shear strain which can be best seen by plotting the corrected stable and unstable stacking fault energies as a function of the shear strain—see Fig. 7 which plots (a) the absolute corrected values and (b) the ratio of the corrected values. For magnetic Ni and for Al, the stacking fault energy increases and the unstable stacking fault energy decreases resulting in an increase in the ratio of unstable to stable stacking fault energy as a function of increasing shear strain.

The difference between the magnetic and nonmagnetic Ni GSFE curves can be qualitatively understood by inspection of the spin resolved charge density as a function of the rigid shift and the use of a simple Stoner picture for itinerant magnetism.<sup>38</sup> Indeed it is observed that the local charge at the stacking fault reaches a maximum at the unstable stacking fault region, which via the Stoner picture would result in the magnetic energy becoming less negative and therefore the total energy of the GSFE curve becoming more positive when compared to the nonmagnetic GSFE curve, as is ob-

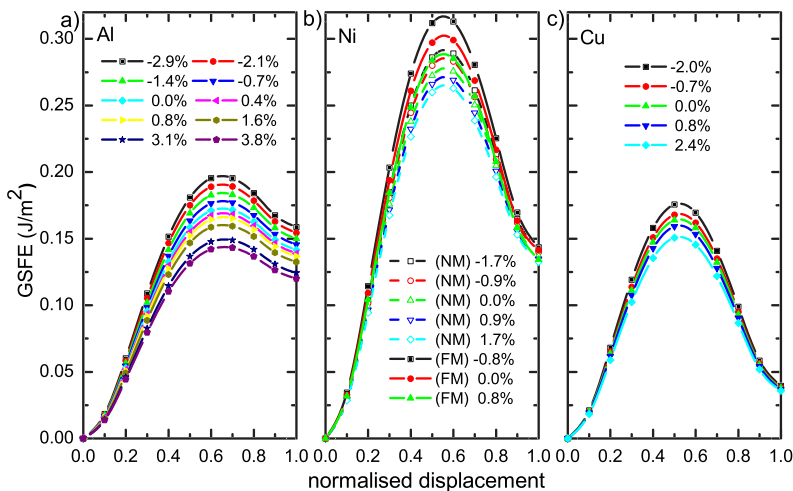


FIG. 3. (Color online) General-stacking-fault energy curves for Al, Ni, and Cu as a function of isotropic volume change. Volume changes are given as percentage changes. For Ni, both the nonmagnetic (NM) and ferromagnetic (FM) phases are shown.

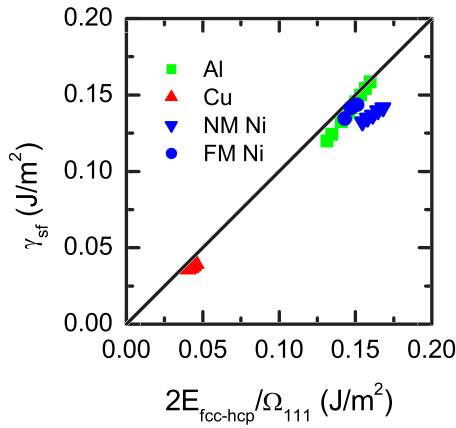


FIG. 4. (Color online) Plot of the calculated stable stacking fault energy versus that derived from the difference between the fcc and hcp phases. For each element, the range of volumes shown in Fig. 3 are used.

served in Fig. 2 for Ni. This is also reflected in a corresponding drop in the local magnetic moment at the slip plane of  $\sim 1\% - 2\%$  in the unstable stacking fault region. The small difference between the magnetic and nonmagnetic stable stacking fault energies is therefore due to the small volume per atom (and therefore the electron density number) difference between the local fcc and hcp structures. The changing contribution in energy due to magnetism across the entire GSFE curve and its strain dependence indicates that a simple rectangular-band Stoner model<sup>39</sup> would be insufficient to describe the ferromagnetism in fcc Ni, and the explicit environmental dependence of the electronic density of states would need to be included in any quantitative model as has been done in (for example) Ref. 40.

### B. Charge density profile and local density of states

Figure 8 shows a view of the unit cell used in the *ab initio* calculation for Al, for three rigid shear configurations: (a) the initial fcc structure, (b) the geometrical unstable stacking fault energy configuration, and (c) the stable stacking fault

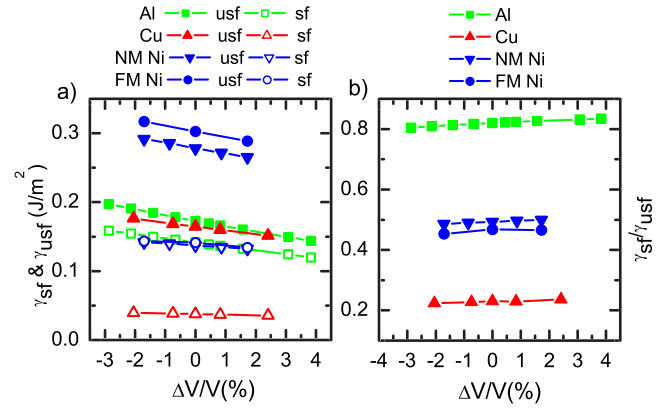


FIG. 5. (Color online) (a) Unstable and stable stacking fault energies and (b) corresponding ratio as a function of volume compression and/or expansion for Al, Cu, and ferromagnetic (FM) and nonmagnetic (NM) Ni.

configuration. Atoms colored blue (shaded darker) in Fig. 8(b) constitute the two central (111) planes of the rigid slip plane. Superimposed on all three figures is a contour map of the converged *ab initio* local electron number density in a plane that is close to a [111] normal. The color (shade) range of the electron number density spans  $0.169/\text{\AA}^3 - 0.219/\text{\AA}^3$ , where intermediate values are colored (shaded) according to the color (shade) bar shown in Fig. 8. The mean valence density for fcc Al is  $0.182/\text{\AA}^3$ , the minimum density at the ionic cores is  $\sim 0.03/\text{\AA}^3$ , and the maximum is  $\sim 0.216/\text{\AA}^3$ . The valence electrons are distributed throughout the fcc structure indicating the strong nearly free electron (NFE) nature of Al. The heterogeneities seen in the charge density are a result of the charge oscillations resulting from the pseudo-potential used and typical for NFE metals. In Fig. 8(b), the geometrical unstable stacking fault configuration, an increased electron number density is seen to occur at the bonds across the slip plane. In terms of the electron density, the surrounding fcc structure is largely unaffected demonstrating once more the short range character of the electronic bonding. In Fig. 8(c), the stable stacking fault configuration, the increased electron number density that was seen in Fig. 8(b)

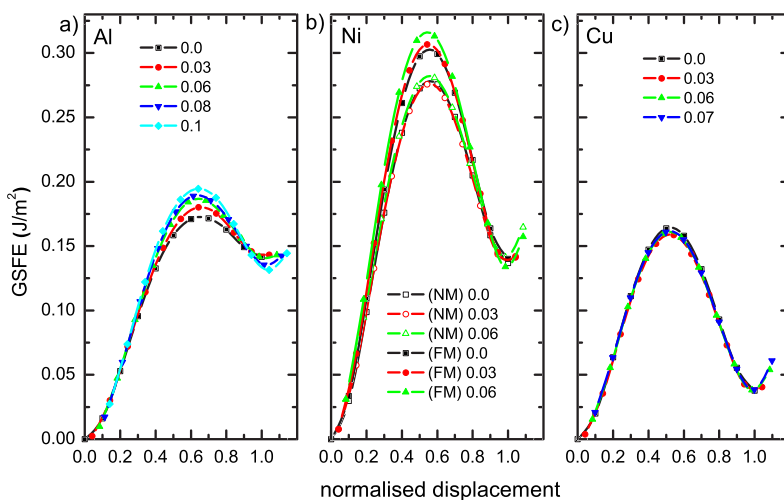


FIG. 6. (Color online) General-stacking-fault energy curves for Al, Cu, and Ni as a function of an applied volume conserving shear strain. For Ni, both the nonmagnetic (NM) and ferromagnetic (FM) phases are shown.

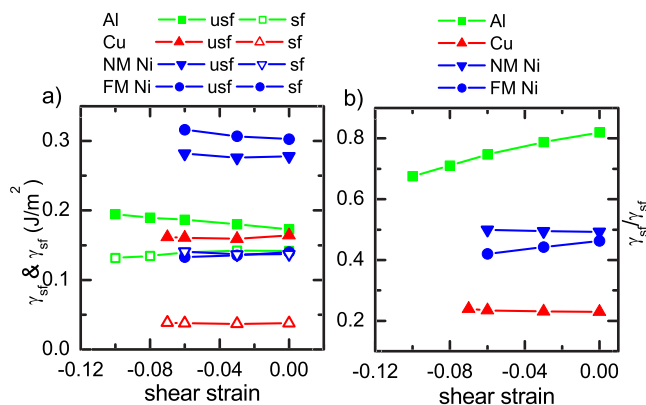


FIG. 7. (Color online) (a) Unstable and stable stacking fault energies and (b) corresponding ratio as a function of an applied volume conserving shear strain for Al, Cu, and Ni.

has disappeared. The differences observed between the upper part of Fig. 8(a) and the upper part of Fig. 8(c), both fcc structures, are due to the fact that after the rigid shift in Fig. 8(c) the charge density plane is halfway between two (111) planes. This artifact also suggests that the hcp structure of the stacking fault in Fig. 8(c) has a larger interstitial region of low electron density—this is, in fact, not the case, the hcp and fcc electron density distributions being not so dissimilar.

Figure 9 shows a similar series of figures for Cu where the electron density is colored and/or shaded over an approximately similar range as in Fig. 8. The mean valence density for fcc Cu is  $0.912/\text{\AA}^3$  reflecting the available 11 electrons per atom. In Fig. 9, the ionic locations exhibit the largest electron number density at  $\sim 15/\text{\AA}^3$  and the interstitial region the least at  $\sim 0.196/\text{\AA}^3$ . This strongly heterogeneous distribution of electrons reflects the well localized atomiclike *d*-state orbitals of the  $\sim 10$  electrons at each ion and the delocalized  $\sim 1$  NFE-like electron within the interstitial region, where the scale of variations of the latter is similar to that seen in Al. The spherical charge distribution around each ion originates from the fully filled *d*-state shell

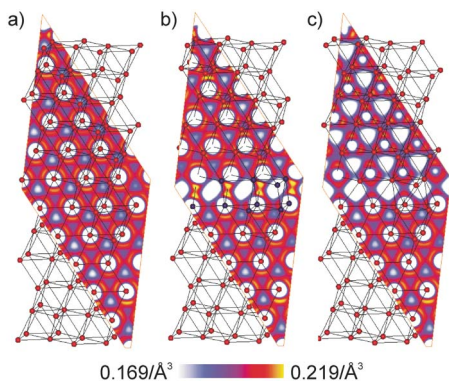


FIG. 8. (Color online) Al atomic structure in (a) initial fcc configuration, (b) geometrical unstable stacking fault configuration, and (c) stable stacking fault configuration. Atoms colored blue (shaded darker) in the central figure indicate the slip plane. For all three configurations the calculated electron density is shown for a (111) plane.

of Cu. Across Figs. 9(a)–9(c), little absolute change is seen in the charge densities. At the geometrical unstable stacking fault configuration [Fig. 9(b)], a slight charge distortion is seen at the slip plane with changes in charge density of the same order as those observed for Al. For Ni (not shown), a similar charge distribution is obtained, with the only difference being that the localized electron number distribution due to the *d*-state electrons is somewhat less spherical reflecting Ni’s unfilled *d*-state shell.

Figures 8 and 9 are in agreement with published work that investigated the nature of ideal shear in Cu and Al,<sup>7</sup> where it was concluded that Al has a directional “stick-rod-like” bonding and Cu has an isotropic “gluelike” bonding. Concerning Al, this viewpoint is, however, not supported when looking at the local DOS of the Al atoms at the slip plane. Figure 10 displays the total local DOS for (a) the initial fcc configuration, (b) the geometrical unstable stacking fault configuration, and (c) the stable stacking fault configuration. Despite the somewhat spiky curves, which arise from the single zone center *k* point along the [111] direction of the unit cell and the resulting 12-fold multiband structure of the Kohn-Sham states, the total local DOS [Fig. 10(a)] is well represented by a the usual square root form apart from the Van Hove singularities close to the Fermi energy. Comparison of the DOS between the three atomic configurations reveals only minor changes just below the Fermi energy as the structure moves from perfect fcc to the stacking fault configuration. The integrated local *s*-, *p*-, and *d*-state resolved densities of states reveal that these differences correspond to changes in relative occupancy of the order of  $\sim 1\%$ – $2\%$  indicating that the actual nature of the hybridization is changing little. If covalency would be at play, more significant changes in the local partial DOSs and their occupancy would be expected. In other words, the increase in the charge density observed in Fig. 8(b) is not an indication of partial covalency but rather is due to the available *s*, *p*, and *d* states that are all only partially filled in the trivalent Al, resulting in unsaturated bonds and Al being a good NFE metal.

The variations in charge density across the GSFE curve seen in Figs. 8 and 9 have also been understood in terms of

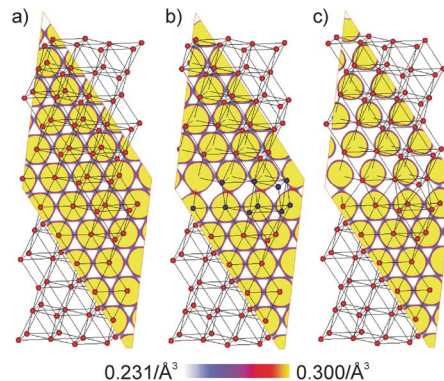


FIG. 9. (Color online) Cu atomic structure in (a) initial fcc configuration, (b) geometrical unstable stacking fault configuration, and (c) stable stacking fault configuration. Atoms colored blue (shaded darker) in the central figure indicate the slip plane. For all three configurations the calculated electron density is shown for a (111) plane.

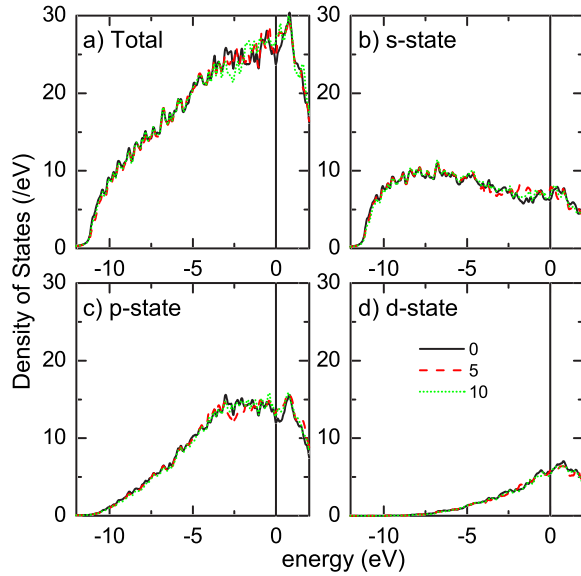


FIG. 10. (Color online) Al local density of states of an atom at the slip plane for the initial FCC configuration (black solid line), the geometrical unstable stacking fault configuration (red dashed line), and the stable stacking fault configuration (green dotted line): (a) displays the total, (b) the  $s$ -state resolved, (c) the  $p$ -state resolved, and (d) the  $d$ -state resolved local densities of states.

the breaking and forming of bond critical points in the charge density, where in the intermediate (unstable stacking fault) region the charge redistributes around the atoms of the slip plane as an emerging cage critical point rather than a bond critical point.<sup>41,42</sup> This has been shown to occur in Al, Ag, and Ir (Ref. 43) and thus is expected to hold also for Cu and Ni—indeed the changes in charge density seen in Figs. 8 and 9 at the unstable stacking fault configuration for Cu and Ni are similar in magnitude to that of Al. Special to Al is that there exists a large anisotropy between the bond breaking and cage forming critical charge densities leading to a strong asymmetry in the GSFE curve for Al (evident in Fig. 2) when compared to other metals.<sup>42</sup> This charge asymmetry is also reflected in Al having an anomalously low elastic anisotropy factor.<sup>41</sup>

### III. DISCUSSION

The relationship  $E_{sf} \approx 2E_{fcc-hcp}$  seen in Fig. 4 evidences the relatively short range electronic nature of the bonding for the metals considered. This result suggests that the unstable stacking fault energy may be well represented by the maximum of the relation between the energy per atom versus a simple shear strain of an fcc lattice along the  $[-1-12]$  direction. Figure 11 displays such a curve for Al together with the unrelaxed and relaxed Al GSFE curves. For direct comparison we plot both quantities as an energy density with units gigapascal. Good correspondence between the maxima of all curves is obtained, where better agreement is seen with the unrelaxed GSFE curve. Such a good correspondence is also seen for Cu and Ni. This approach has also been developed in Ref. 7 in which the multiplane generalized stacking fault

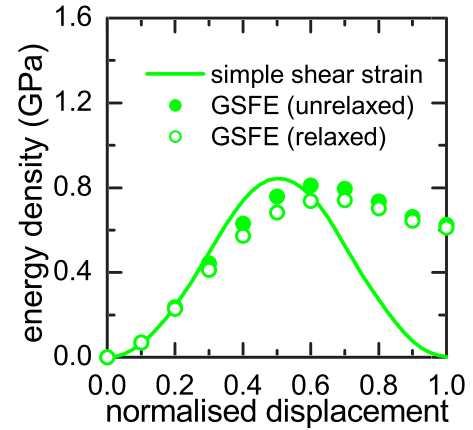


FIG. 11. (Color online) The energy increase per atom as a function of deforming the fcc lattice under simple shear strain conditions for Al. For comparison, the unrelaxed and relaxed Al GSFE curves are also shown.

energy,  $\gamma_n(x)$ , was calculated, where  $\gamma_1(x)$  is equivalent to the GSFE curves shown in Fig. 1 and  $\gamma_\infty(x)$  represents the energy of globally sheared fcc lattice. In that work, however, a simple shear stress was used rather than a simple shear strain to better investigate more realistic deformations that measure strength.

Figure 12(a) now displays the corresponding simple shear strain curves for Al, Ni, and Cu. By plotting the energy curves in this way, the curvature at a displacement of zero (and unity) is equal to the shear modulus along the  $[-1-12]$  slip direction. Figure 12(b) plots the obtained shear moduli as a function of the energy density maximas in Fig. 12(a) (filled circles) and the unstable stacking fault energies (open circles). The linear correspondence is good for Cu and Ni, demonstrating that the shear modulus plays an important role in the energy scale of the unstable stacking fault. This is a more general manifestation of the classical notion that elasticity is a first order determinant of material strength. The fact that Al does not lie on the same line, confirms that elasticity underestimates the unstable stacking fault energy for this metal.<sup>7</sup>

Such a simple picture of the unstable stacking fault region of the GSFE curve for Cu, Ni, and to a lesser extent Al then

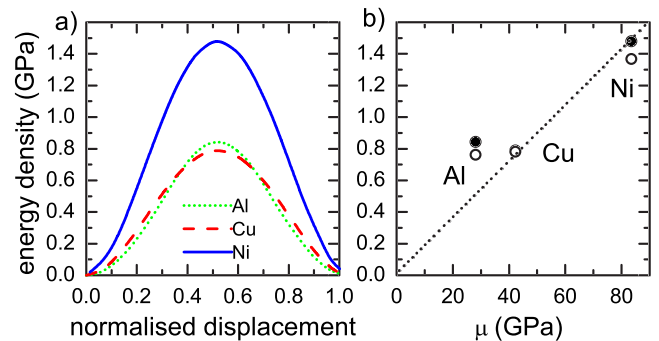


FIG. 12. (Color online) (a) Shear strain energy curves divided by atomic volume. (b) Maximum of shear strain energy curves (filled circles) and unstable stacking fault energy (open circles) as a function of calculated shear modulus.

suggests that its response to strained environments will largely be determined by how the elastic constants vary as a function of a finite lattice distortion. In other words, the third order elastic constants control the behavior of the GSFE curves in Figs. 3 and 5–7 of the unstable stacking fault region. For the case of isotropic volume expansion and contraction, simple analytical formulas exist for expressing the derivative of the cubic elastic constants with respect to pressure.<sup>44</sup> Using these relations, the derivative of the shear modulus with respect to pressure can be obtained in terms of the second and third order elastic constants. Using the third order constants derived from a recent multivariate linear regression analysis of a wide range of published data,<sup>45</sup> we obtain experimental  $d\mu/dP$  values of  $1.55\pm 0.10$ ,  $1.06\pm 0.23$ , and  $1.46\pm 0.25$  for, respectively, Al, Cu, and Ni. By exploiting the linear relationship between simple shear strain energy density and the calculated shear modulus seen in Fig. 12(b) and expressing the volume changes of Fig. 3 as a hydrostatic pressure (using the DFT calculated bulk modulus), we obtain values of  $d\mu/dP$  for Al, Cu, and Ni equaling 2.44, 1.12, and 1.05, which compare well with those estimated via third order elasticity. Cu exhibits the best agreement, followed by Ni and Al. We note that since Ni has an unstable stacking fault energy less than that predicted by elasticity, its value of  $d\mu/dP$  will be less than that predicted by third order elasticity, whereas for Al it will be larger—as is demonstrated in the present numerical values. Such an approach could be applied to the unstable stacking fault energy dependence of the volume conserving simple shear strain by calculating the derivative of the shear modulus with respect to such a distortion; however, it appears that no such analytical formulas exist yet in the literature.

#### IV. CONCLUDING REMARKS

The motivation for the present work has been to investigate how the stacking fault energy curve is affected by large isotropic and volume conserving shear strains of the lattice. The *ab initio* methods applied show that there are only minor changes in the GSFE curves for Al, Cu, and Ni for the applied distortions, strengthening the notion that the ratio between stable and unstable stacking fault energy provides qualitative physical insight into the nature of slip in nanocrystalline materials where highly distorted environments are present.<sup>18</sup> The present work has shown that for Cu, the form of the GSFE curve and its behavior under strain can be very well understood in terms of second and third order elasticities and its value for  $E_{\text{fcc-hcp}}$ . For Al and Ni, a significant part of the GSFE curve can also be understood in terms of these bulk material parameters, although in the case of Al the deviations away from such a simple model are significant

enough to result in anomalous strength properties as investigated in Refs. 7 and 8.

The simulation of multimillion atom *nc* atomic configurations must employ less accurate empirical potential schemes such as the embedded atom or second moment tight binding formalisms to model the metallic bond which do not take into account explicitly angular bonding. The present results demonstrate that for the accurate empirical simulation of the GSFE curve, such interatomic models must be able to describe well the energy difference,  $E_{\text{fcc-hcp}}$ . In practice the fitting of this energy difference is achieved by extending the range of a potential to more distant neighbors. While this is an effective approach, it is inconsistent with the short range nature of, for example, the *d*-state bond and leads to transferability issues when the potential is applied to atomic configurations not included in the fitted physical database. A typical configuration not included in such a database is the unstable stacking fault. A good example of this is in the Al and Ni embedded atom potentials of Mishin *et al.* which in one case employ spline functions<sup>46</sup> and in another case use conventional analytical functions.<sup>47</sup> All of these potentials have been fitted to  $E_{\text{fcc-hcp}}$  and reproduce well the stable stacking fault energy, with the range of these potentials extending to up to the fifth nearest neighbor shell. For the predicted unstable stacking fault energy, the two representations for both Al and Ni give, however, different values with the spline representation in Ref. 46 agreeing better with the *ab initio* predictions than the analytical functional representation in Ref. 47. In terms of strained GSFE curves, the present work also demonstrates the importance of third order elastic constants suggesting that such anharmonic material properties should also be included in the fitting database of future empirical potentials.

In conclusion, the present work demonstrates a relative insensitivity of the stable to unstable stacking fault ratio to an isotropic volume change and a volume conserving simple shear. In the context of the work performed in Ref. 18, this indicates that the logical arguments therein remain valid in strongly strained environments such as near a grain boundary region. Therefore the explanation of why only partial dislocations are seen in molecular dynamics simulations of the deformation properties of *nc*-Cu and *nc*-Ni, and full dislocation in *nc*-Al, is on a firmer theoretical grounding. The work has also provided insight into the origins of the generalized stacking fault energy curves in terms of a metal's second and third order elastic properties.

#### ACKNOWLEDGMENT

The authors acknowledge the financial support of European Commission (FP6-NANOMESO, Grant No. 016710) for financial support.

- <sup>1</sup>V. Vitek, *Phys. Status Solidi* **18**, 687 (1966).
- <sup>2</sup>V. Vitek, *Philos. Mag.* **18**, 773 (1968).
- <sup>3</sup>J. Frenkel, *Z. Phys.* **37**, 572 (1926).
- <sup>4</sup>J. R. Rice, *J. Mech. Phys. Solids* **40**, 239 (1992).
- <sup>5</sup>D. Roundy, C. R. Krenn, M. L. Cohen, and J. W. Morris, *Phys. Rev. Lett.* **82**, 2713 (1999).
- <sup>6</sup>C. R. Krenn, D. Roundy, J. W. Morris, and M. L. Cohen, *Mater. Sci. Eng., A* **A317**, 44 (2001).
- <sup>7</sup>S. Ogata, J. Li, and S. Yip, *Science* **298**, 807 (2002).
- <sup>8</sup>S. Ogata, J. Li, N. Hirotsuki, Y. Shibutani, and S. Yip, *Phys. Rev. B* **70**, 104104 (2004).
- <sup>9</sup>H. Van Swygenhoven, *Science* **296**, 66 (2002).
- <sup>10</sup>J. Schiøtz, F. D. Di Tolla, and K. W. Jacobsen, *Nature (London)* **391**, 561 (1998).
- <sup>11</sup>J. Schiøtz and K. W. Jacobsen, *Science* **301**, 1357 (2003).
- <sup>12</sup>W. Yamakov, D. Wolf, S. R. Phillpot, and H. Gleiter, *Acta Mater.* **51**, 4135 (2003).
- <sup>13</sup>H. Van Swygenhoven, P. M. Derlet, and A. Hasnaoui, *Phys. Rev. B* **66**, 024101 (2002).
- <sup>14</sup>P. M. Derlet, H. Van Swygenhoven, and A. Hasnaoui, *Philos. Mag.* **83**, 3569 (2003).
- <sup>15</sup>H. Van Swygenhoven, P. M. Derlet, and A. G. Frøseth, *Acta Mater.* **54**, 1975 (2006).
- <sup>16</sup>Ž. Budrović, H. Van Swygenhoven, P. M. Derlet, S. Van Petegem, and B. Schmidt, *Science* **304**, 273 (2004).
- <sup>17</sup>S. Brandstetter, Ž. Budrović, S. Van Petegem, B. Schmitt, E. Stergar, P. M. Derlet, and H. Van Swygenhoven, *Appl. Phys. Lett.* **87**, 231910 (2005).
- <sup>18</sup>H. Van Swygenhoven, P. M. Derlet, and A. G. Frøseth, *Nat. Mater.* **3**, 399 (2004).
- <sup>19</sup>A. G. Frøseth, P. M. Derlet, and H. Van Swygenhoven, *Acta Mater.* **52**, 2259 (2004).
- <sup>20</sup>A. G. Frøseth, P. M. Derlet, and H. Van Swygenhoven, *Acta Mater.* **52**, 5863 (2004).
- <sup>21</sup>J. D. Honeycutt and H. C. Andersen, *J. Phys. Chem.* **91**, 4950 (1987).
- <sup>22</sup>J. Cormier, J. M. Rickman, and T. J. Delph, *J. Appl. Phys.* **89**, 99 (2001).
- <sup>23</sup>P. M. Derlet, S. Van Petegem, and H. Van Swygenhoven, *Phys. Rev. B* **71**, 024114 (2005).
- <sup>24</sup>G. Kresse and J. Hafner, *Phys. Rev. B* **47**, RC558 (1993).
- <sup>25</sup>G. Kresse and J. Furthmüller, *Phys. Rev. B* **54**, 11169 (1996).
- <sup>26</sup>M. Methfessel and A. T. Paxton, *Phys. Rev. B* **40**, 3616 (1989).
- <sup>27</sup>P. J. H. Denteneer and J. M. Soler, *Solid State Commun.* **78**, 857 (1991).
- <sup>28</sup>J. Hartford, B. von Sydow, G. Wahnström, and B. I. Lundqvist, *Phys. Rev. B* **58**, 2487 (1998).
- <sup>29</sup>J. A. Zimmerman, H. Gao, and F. F. Abraham, *Modell. Simul. Mater. Sci. Eng.* **8**, 103 (2000).
- <sup>30</sup>G. Lu, N. Kioussis, V. V. Bulatov, and E. Kaxiras, *Phys. Rev. B* **62**, 3099 (2000).
- <sup>31</sup>Y. Sun and E. Kaxiras, *Philos. Mag. A* **75**, 1117 (1997).
- <sup>32</sup>A. Wright, M. S. Daw, and C. Y. Fong, *Philos. Mag. A* **66**, 387 (1992).
- <sup>33</sup>N. M. Rosengaard and H. L. Skriver, *Phys. Rev. B* **47**, 12865 (1993).
- <sup>34</sup>A. G. Frøseth, R. Holmestad, P. M. Derlet, and K. Marthinsen, *Phys. Rev. B* **68**, 012105 (2003).
- <sup>35</sup>M. W. Finnis, *Interatomic Forces in Condensed Matter* (Oxford University Press, Oxford, 2003), pp. 197–198.
- <sup>36</sup>D. G. Pettifor, *Bonding and Structure of Molecules and Solids* (Oxford University Press, Oxford, 1996), Chap. 6.
- <sup>37</sup>A. K. McMahan and J. A. Moriarty, *Phys. Rev. B* **27**, 3235 (1983).
- <sup>38</sup>E. C. Stoner, *Proc. R. Soc. London, Ser. A* **169**, 339 (1939).
- <sup>39</sup>D. G. Pettifor, *J. Magn. Magn. Mater.* **15**, 847 (1980).
- <sup>40</sup>N. C. Bacalis, N. Theodorakopoulos, and D. A. Papaconstantopoulos, *Phys. Rev. B* **55**, 11391 (1997).
- <sup>41</sup>M. E. Eberhart, *Acta Mater.* **44**, 2495 (1996).
- <sup>42</sup>M. E. Eberhart, *Phys. Rev. Lett.* **87**, 205503 (2001).
- <sup>43</sup>N. Kioussis, M. Herbranson, E. Collins, and M. E. Eberhart, *Phys. Rev. Lett.* **88**, 125501 (2002).
- <sup>44</sup>D. J. Dunstan and S. H. B. Bosher, *Phys. Status Solidi B* **235**, 396 (2003).
- <sup>45</sup>A. S. Johal and D. J. Dunstan, *Phys. Rev. B* **73**, 024106 (2006).
- <sup>46</sup>Y. Mishin, D. Farkas, M. J. Mehl, and D. A. Papaconstantopoulos, *Phys. Rev. B* **59**, 3393 (1999).
- <sup>47</sup>Y. Mishin, D. Farkas, M. J. Mehl, and D. A. Papaconstantopoulos, *MRS Symposia Proceedings No. 538* (Materials Research Society, Pittsburgh, 1999), p. 535.